photonics

MDPI

Article

Divergence of Long-Range Bessel-Gaussian Beams with Truncated Coaxial Rings

Nikolay Dimitrov [1,*], Maya Zhekova [1] and Alexander Dreischuh [1,2,3]

[1] Department of Quantum Electronics, Faculty of Physics, Sofia University "St. Kliment Ohridski", 1164 Sofia, Bulgaria; mzhekova@phys.uni-sofia.bg (M.Z.); ald@phys.uni-sofia.bg (A.D.)
[2] National Centre of Excellence Mechatronics and Clean Technologies, 1756 Sofia, Bulgaria
[3] Bulgarian Academy of Sciences, 1040 Sofia, Bulgaria
* Correspondence: nrd@phys.uni-sofia.bg

Abstract

Bessel beams, one of the four known types of beams that are exact solutions of the Helmholtz equation, are remarkable with their non-diffracting nature. In reality, generated with real (Gaussian) laser beams with finite transverse profiles, Bessel-Gaussian beams (BGBs) are quasi-non-diffracting and remarkably stable against spatial perturbations. Quasi-non-diffracting means that the central peaks of the BGBs typically have divergences of the order of microradians. Here, we present experimental evidence that the truncation of the concentric rings surrounding the central peak of the long-range BGBs has a pronounced and controllable effect on the divergence of their peaks. The method is well suited for microradian divergences and has a minimal effect when the divergence of the BGB approaches one milliradian. The truncation of the rings of the BGBs could be applied, for example, in free-space communications, in locating a receiver station with a more divergent beam, after which the spreading of the central peak in space could be reduced to ensure a more secure data transfer.

Keywords: Bessel beam; Bessel-Gaussian beam; quasi-non-diffracting beam; beam divergence; beam truncation

1. Introduction

Generally speaking, spatially confined waves experience significant diffraction broadening when propagating freely. This is not the case for Bessel beams (BBs). Together with the infinite plane waves, the Airy and Ince beams, each in its respective coordinate system, are exact solutions of the Helmholtz equation [1,2]. Mathematically, zero-order BB consists of a central peak surrounded by an infinite number of concentric rings with decreasing amplitudes. These satellite rings are separated from each other by radial π-phase jumps (see, e.g., Figure 14 in [3]). In an m-th order BB, the central peak is doughnut-shaped and carries an optical vortex with topological charge m (i.e., a point phase dislocation surrounded by a spiral wavefront; [3]). Mathematically perfect BBs are non-diffracting, but cannot be generated in practice. Due to the finite transverse dimensions of the laser beams used (e.g., Gaussian beams), the number of satellite rings of the central peak is finite, and the beams are referred to as Bessel-Gaussian beams (BGBs). They are characterized by their low diffraction angles (typically of the order of microradians; see, e.g., [4,5]), which are orders of magnitude lower than those of the undisturbed (e.g., Gaussian) beams used to form them. For the reasons mentioned above, the actually generated Bessel-type beams are referred to as quasi-non-diffracting BGBs.

Received: 24 March 2026
Revised: 27 April 2026
Accepted: 9 May 2026
Published: 13 May 2026

However context dependent, based on their length of propagation, BGBs can be classified as short- and long-range ones. Short-range BGBs are typically generated by the interference of selected/split parts of the incoming laser beam with, e.g., ring-shaped diaphragms in the rear focal planes of lenses [6–9] or using axicons [9–12]. The typical propagation distances of such beams are on the order of millimeters and units of centimeters. Since the angular spectrum of the Bessel function is a ring, long-range BGBs can be generated by Fourier-transforming ring-shaped beams in space by focusing them with thin lenses [5,13–15]. The typical propagation distances of such BGBs extend over meters. Of course, the distinction is conditional. For example, an axicon doublet consisting of a positive and a negative axicon with high and low refractive indices, respectively, has recently been demonstrated to generate a Bessel-like beam propagating more than 200 m [16]. Logically, the characteristic propagation lengths of BGBs determine the areas of their applicability—from optical microscopy [17], optical trapping, and tweezing of particles [18,19], high aspect ratio (length/diameter) nanochannel machining, photopolymerization, nanopatterning [20–25], and generation of Bessel-Gaussian attosecond pulse trains in the extreme ultraviolet [26], to real-world free-space optical communications [27,28], just to mention a few.

The measurements in this work are conducted using long-range Bessel-Gaussian beams generated by Fourier-transforming in space ring-shaped coherent beams with large ring radius-to-arc width ratio (e.g., $r_0/\omega_0 \geq 10$) [5,13–15]. The use of optical vortices (OVs) is essential since they produce ring-shaped intensity distributions with dark cores when imposed on a Gaussian beam. OVs have spiral phase wavefronts characterized by their topological charge (TC)—a positive or negative integer number m corresponding to the total phase change $2\pi m$ over the azimuthal coordinate (see, e.g., Figure 3 in [3]). A ring-shaped beam with the desired large ratio r_0/ω_0 is generated by creating OVs with a high topological charge m on an input Gaussian laser beam (see, e.g., Figure 2a in [13]). Due to their decay into m optical vortices with unit TCs and their mutual repulsion, a tiny ring-shaped beam with a wide dark core is formed. The higher the initially formed TC m, the wider the radius of the bright ring of the beam r_0 and the tinier its arc width w_0. The next step is to erase the optical vortices. Both their formation and annihilation can be achieved, for example, by reflections from appropriately programmed liquid crystal phase modulators (see, e.g., Figure 2a in [13]) or by passing the beam through appropriately oriented vortex phase plates (VPs) [5,15]. By appropriately "programmed/oriented" we mean programming the phase modulators and orienting the VPs so that the vortices are first generated with TCs m and then erased with OVs with opposite TCs ($-m$). (If an l-th order BGB is to be generated, the numbers of the generated and annihilated OVs should differ by $|l|$). The resulting ring-shaped beam with a large dark core and a flat phase front is focused with a thin lens. As a result, a Bessel-Gaussian beam can be observed at meters after the focal plane of the lens. The basic analytical model for the generation of BGBs by annihilating multiple-charged optical vortices is published [13]. It is essential in this model to approximate an exponent of the type $\exp[2rr_0/\omega_0^2]$ by a modified Bessel function of the first kind $I_l[2rr_0/\omega_0^2]$, which holds for $r_0 \gg \omega_0$.

The "needle beams" are a particular kind of truncated Bessel beams—fringe-free, free space, optical Bessel-like beams with typical transversal dimensions on micrometer scale [29]. The generation of Bessel-like needle beams by axicons is based on the composition of a sequence of converging partial beams. An interesting property of such beams is their robustness against angular tilt [30]. Although their characteristic propagation lengths are on the order of a few centimeters or less, with such beams, aspect ratios of $>10^5$ can be achieved. A precise overview of the physics and applications of needle beams is provided in [29]. The goal of this analysis, however, is different.

To the best of our knowledge, in the literature there are no systematic data on the influence of a reduced number of satellite rings on the diffraction spreading of the central peak of long-range Bessel-Gaussian beams. Let us recall that ideal (in the mathematical sense) BBs do not diffract, while realistically generated (with a finite number of satellite rings) BGBs have diffraction angles in the microradian range. It can be assumed that, at one and the same distance, the increasing truncation of the rings surrounding the central peak will lead to its larger transverse broadening. Such control of the spreading of a laser beam in space, if possible without any moving optical elements, would probably find applications. We would imagine that one such application would be in the long-range free-space communication—e.g., to locate a receiver station with a more divergent beam, after which to reduce its transverse spreading to ensure a more secure data transfer. In this article, we report experimental results on the divergences of long-range Bessel-Gaussian beams with truncated coaxial rings. Truncated BGB (TBGB) with n rings means the (n + 1)-th dark ring and all beyond are truncated by an, e.g., iris diaphragm.

2. Experimental Data and Discussion

The experimental setup we used for measuring the divergences of the central peaks of the truncated Bessel-Gaussian beams (TBGBs) is shown in Figure 1. With a set of diaphragms and mirrors the beams of the different used lasers are directed along the same propagation path so that changing them does not require readjustment of the rest of the setup. We used a vortex phase plate (VP) designed and fabricated for 800 nm with a topological charge $|TC| = 8$. Laser beams at wavelengths of 430 nm, 800 nm, and 1100 nm were generated separately by selecting them from the tunable picosecond emission of a supercontinuum laser (SuperK Fianium, NKT Photonics, Birkeroed, Denmark). For comparison, at a central wavelength of 800 nm, beams/pulses from a mode-locked sub-7 fs Ti:Sapphire-based laser oscillator (Element 2, Spectra-Physics, Vienna, Austria) were also used. With this choice of wavelengths, we ensured (a) relatively narrow-bandwidth and broadband radiation corresponding to the design central wavelength of 800 nm of the VP; (b) illumination at a wavelength (430 nm) as close as possible (for the Fianium laser) to the second harmonic of the VP's design wavelength, generating/annihilating 16-fold charged OVs with fractional TC; and (c) longer wavelength radiation (1100 nm), generating/annihilating OVs with fractional OVs with lower TCs.

The particular laser beam passes first through the stationary VP. After two reflections from mirrors M1 and M2, it passes in reverse direction through the same VP. As a result, first, a doughnut-shaped OV with, e.g., "positive" TC is formed, and then the 8 decayed OVs are annihilated by the same number of OVs with "negative" TCs. At the exit of this double-pass configuration, a ring-shaped beam with a flat phase front is prepared. The Fourier transformation in space is performed by a lens of a focal length $f = 50$ cm. The focal length of the lens is chosen for convenience. Its position is determined by the condition that the size of the ring-shaped beam in the second pass is close to that of the incoming beam in the plane of the VP, so that the topological charges of the vortices can be successfully annihilated. The particular distances are listed in the caption of Figure 1. The CCD camera was moved to different positions along the propagation path of the BGBs to a maximum distance of 470 cm, measured from the location of the lens focal plane LFP.

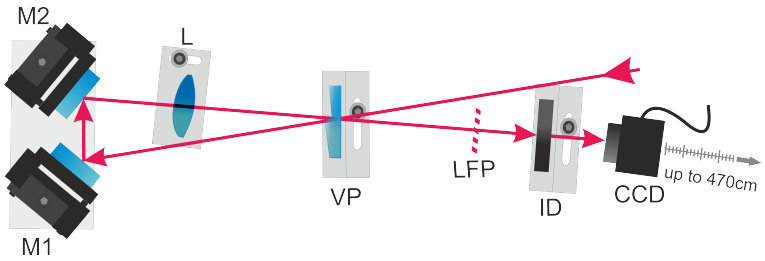

Figure 1. Experimental setup. VP—vortex phase plate, fabricated to produce optical vortices with topological charge $|TC| = 8$. L—fused silica lens ($f = 50$ cm). M1, M2—flat silver-coated mirrors. LFP—lens focal plane. ID—iris diaphragm. CCD—movable charge-coupled device camera. The corresponding distances are: VP to M1—32 cm; M1 to M2—6 cm; M2 to L—13 cm; L to LFP, when using $f = 50$ cm—about 65 cm. LFP to ID—25 cm (when the beam waist of the incoming Gaussian beam is offset from the front focal plane of a thin lens (at 1.5 m in our case), the waist of the focused beam is offset from the back focal plane of the lens as well (estimated offset 14 cm)). All positions of the CCD camera are measured from the LFP.

In Table 1, we summarize the measured divergence half angles of the central peaks of a Bessel-Gaussian beam (BGB) and of truncated BGBs (TBGBs) with 3, 2, and 1 satellite dark and bright ring(s) for the mentioned wavelengths. (TBGB with n satellite dark/bright rings means that the iris diaphragm is truncating the $n + 1$-st dark ring and the further lying bright and dark rings.) Notations (ps) and (7 fs) refer to the use of relatively narrow-bandwidth tunable picosecond emission extracted from the supercontinuum laser emission and to the broadband pulses of the mode-locked femtosecond laser oscillator, respectively. The significantly higher divergence of the unmodulated background Gaussian beam is included on the right part of the table as well. The data for the broadening of the central peak of the BGBs obtained at the design wavelength of the VP (800 nm) with picosecond (ps) and femtosecond (fs) pulses are very close. They differ minimally, by about 5 μrad. With 3 and 2 satellite rings remaining in the TBGBs, the differences between fs and ps beams increase to about 45 μrad. When only 1 ring is intentionally left, the difference reaches about 90 μrad. Except for the undisturbed BGBs, the divergences of the truncated femtosecond (broad bandwidth) beams are higher than those of the truncated (relatively short-bandwidth) picosecond beams. The latter we attribute to the observed "coloring" of the outermost rings of unperturbed femtosecond BGBs (see Figure 5 in [5]). The physical mechanism behind it is the stronger pronounced diffraction of the longer-wavelength components of the broad bandwidth spectrum, which is weaker for the shorter-wavelength components.

From the data in Table 1, for the 800 nm (ps) case, the divergence of the untruncated BGB is 100 (±1) μrad, while after truncation to three rings, it decreases to 94 (±7) μrad. In view of the relatively large error bars ((±7) μrad and (±1) μrad), we consider this anomalous observation as an artifact.

From Table 1, it is also clear that the femtosecond Gaussian beam has nearly twice higher divergence compared with the maximally truncated BGB. It is also interesting to note that the undisturbed picosecond background beam has an almost 10 times higher divergence than the maximally truncated picosecond BGB. This is due to the transfer of the beams from the picosecond tunable source (Fianium) to the experiment via an optical fiber.

At a wavelength of 430 nm, the BGB has a divergence that is half that at 800 nm. The result is not surprising. It is due to the fact that the generated (and annihilated) OVs have a topological charge that is twice as high as at 800 nm, which leads to a significantly larger radius of the ring-shaped beam before its Fourier transform (see Figure 2b in [13]) and to a larger number of satellite rings after the formation of the BGB (see Figure 1 in [14]). When the satellite rings are reduced to 3, 2, and 1, the divergence of the TBGB increases nearly

2, 3, and 4 times, respectively. Even the highest divergence remains about 7.5 times lower than that of an undisturbed Gaussian beam at the same wavelength.

The other extreme case studied here is the generation of a BGB and of TBGBs at a wavelength of 1100 nm. Due to the smaller radius of the ring-shaped beam before its Fourier transformation $r_0/\omega_0 = 8$ (the condition $r_0/\omega_0 \geq 10$ is violated; see Equation (7) in [13] and the comment in section Introduction), only a well-formed central peak and one first satellite ring are observed, surrounded by highly structured ring-shaped formations. The second reason for this unsatisfactory quality of the BGB at 1100 nm is that, in front of the focusing lens, the vortex ring is strongly azimuthally modulated (see Figure S5 in the Supplementary Materials). Because of this, two of the cases studied at the other wavelengths are marked as not available (n.a.) in the last row of Table 1. It can be seen that the shaped Bessel-Gaussian-like beam has the highest divergence, which further increases about 1.7 times when the outer-lying structured formations are cut off. The divergence of the undisturbed background beam is measured to be more than one and a half orders of magnitude higher, and it is the highest of all undisturbed background beams.

Based on the data summarized in Table 1, it can be concluded that the truncation of the concentric rings surrounding the central peak of the long-range BGBs has a pronounced and controllable effect in increasing the divergence of their central peaks.

Table 1. Divergences of the central peaks of Bessel-Gaussian beam (BGB) and of truncated BGBs (TBGBs) with 3, 2, and 1 satellite ring(s) for four different wavelengths. The standard errors of the respective linear fits are given in brackets. Missing standard errors for the divergences of the pure background beams means that only two beam energy densities could be recorded and the linear fit of the data is used.

Divergence Half-Angle (μrad) for $f = 50$ cm					
Wavelength	**BGB**	**3 Rings**	**2 Rings**	**1 Ring**	**Background Beam**
430 nm (ps)	48 (±1)	81 (±4)	139 (±2)	196 (±5)	1500
800 nm (ps)	100 (±1)	94 (±7)	165 (±6)	207 (±4)	2000
800 nm (fs)	95 (±2)	140 (±2)	201 (±7)	300 (±13)	570 (±7)
1100 nm (ps)	129 (±2)	n.a.	n.a.	216 (±6)	3800

In Figures 2 and 3, following one and the same style of presentation, we show results obtained with relatively narrow-bandwidth picosecond laser pulses (Figure 2) and with broad bandwidth 7 fs pulses (Figure 3). Intentionally, in both cases the central wavelength of the spectra of the laser beams was $\lambda = 800$ nm in order to match the wavelength for which the VP was fabricated to produce OV with a $|\mathrm{TC}| = 8$. The difference that could be observed in the data extracted from the two series of measurements could be due to two factors—the significantly wider spectra of the femtosecond pulses (>300 nm at 10 dB level) and the significantly higher broadening of the background picosecond beam transported to the experimental setup with an optical waveguide. The spectral components of the femtosecond beam lying farther away from 800 nm are expected to cause the generation/decay/interaction and, finally, the annihilation of OVs with fractional TCs. In our previous experiments, we showed [14,16] that VPs produced for a particular wavelength can also be used at significantly different wavelengths, including with femtosecond pulses; i.e., the approach used to generate BGBs is tolerant of the used wavelengths. Taking a closer look at the middle two rows of Table 1, it can be seen that when carrying all their satellite rings, the BGBs have practically identical divergences in both picosecond and femtosecond modes (100 (±1) μrad in picosecond mode and 95 (±2) μrad in femtosecond mode). Truncating their satellite rings to 3, 2, and 1 results in a noticeably larger increase in the divergence of the central peak—e.g., 300 (±13) μrad in femtosecond mode versus

207 (±4) μrad in picosecond mode, when the beams carry only one satellite ring around their central peaks.

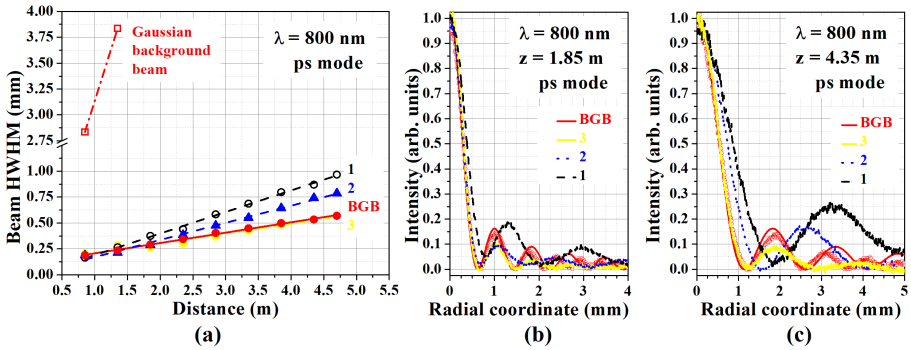

Figure 2. Results obtained with narrow-bandwidth (picosecond) laser beam at λ = 800 nm using a vortex plate (VP) fabricated to produce OV with a |TC| = 8 at 800 nm. (**a**)—Beam divergences of the generated BGBs (red solid circles) and of the TBGBs with 3 (yellow line), 2 (blue dashed line and solid triangles), and 1 satellite dark ring (black dashed line and open circles). The significantly higher divergence of the unmodulated Gaussian background beam is seen in the upper-left part of the graph. (**b**,**c**)—Normalized radial cross-sections of the BGB and of the TBGBs for propagation distances z = 1.85 m and z = 4.35 m behind the lens focal plane.

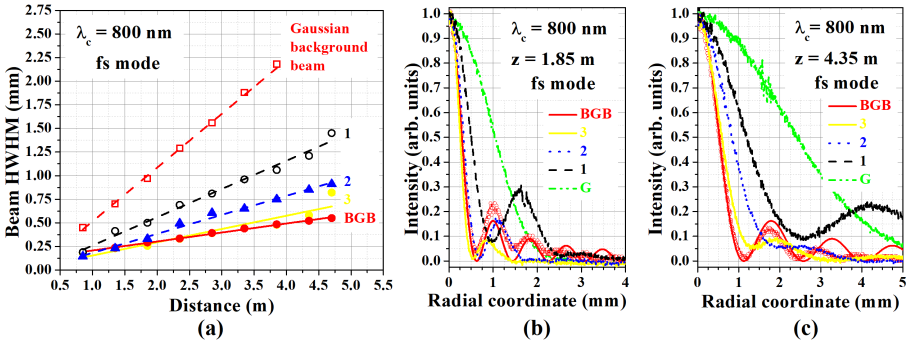

Figure 3. Results obtained with broad bandwidth 7 fs pulses and laser beam at a central wavelength of its spectrum λ = 800 nm. VP fabricated to produce OV with a |TC| = 8 at 800 nm is used. (**a**)—Beam divergences of the generated BGB (red solid circles) and of the truncated BGBs with 3 (yellow line and solid circles), 2 (blue dashed line and solid triangles), and 1 satellite dark ring (black dashed line and open circles). The dash-dotted line is showing the significantly higher divergence of the unmodulated Gaussian background beam. (**b**,**c**)—Normalized radial cross-sections of the BGB and the TBGBs for propagation distances z = 1.85 m and z = 4.35 m behind the lens focal plane. The respective cross-section of the Gaussian background beam (G) is shown as well.

Nonetheless, the trend of increasing the diffraction of the central peak with the stronger truncation of the satellite rings is well expressed in both cases, as can be seen in panels (a) of Figures 2 and 3. Following the same style of presentation, panels (a) show the beam divergences of the generated BGBs (red solid circles) and of the truncated BGBs with 3 (yellow line and solid circles), 2 (blue dashed line and solid triangles), and 1 satellite ring (black dashed line and open circles). The dash-dotted lines show the much higher divergence of the unmodulated Gaussian background beam. The linear dependence of the beam expansion with increasing distance is clearly expressed. The difference between the changing size of the central peak of the BGB when it carries all its satellite rings and when their number is reduced to 3 rings is minimal. At this stage, it could be concluded that cutting out the satellite rings down to 3 allows the TBGB to propagate as if it were an untruncated BGB.

The used fitting function we defined as $AJ_0^2[\rho(x - x_0)]\exp\{-(x - x_0)^2/w^2\} + B$, where J_0 is a Bessel function of the first kind of order zero, depending on the spatial

coordinate x with an eventual offset x_0. The scaling factor ρ in the Bessel function argument is inversely proportional to the width of the central peak. The smaller the width w of the Gaussian envelope, the less concentric rings are clearly seen around the central peak of the BGB. A and B are the amplitude scaling factor and the eventual constant background offset, respectively.

In panels (b) and (c), in Figure 2 for picosecond mode and in Figure 3 for femtosecond mode, we show normalized radial cross-sections of the BGBs and the TBGBs for propagation distances z = 1.85 m (panels (b)) and z = 4.35 m (panels (c)) behind the Fourier-transforming lens L. The color coding of the curves is kept the same as in panels (a) of both graphs. The experimental data for the radial distributions of the BGB intensity (hollow red circles) show that the positions of the peaks of the first two satellite rings match well with those of the theoretical approximations with squared Bessel-Gaussian functions (red solid curves). With three dark rings cut off, the widths at the central peaks are practically unchanged at z = 1.85 m and only slightly increased at z = 4.35 m. Reducing the satellite rings to 2 significantly widens the peak at the greater distance z = 4.35 m. With only one satellite ring preserved, the broadening of the central peak is clearly noticeable at both distances, as is the increased energy transfer to the first outer satellite ring. We attribute this to the probable loss of radial π-phase modulation when filtering only one satellite ring, as indicated by the lack of modulation of the intensity to zero (see the black curves in graphs (b) and (c) in Figures 2 and 3).

From the above, it can be concluded that (*i*) the truncation of the satellite rings surrounding the central peak of the BGBs leads to an increase in their divergences. (*ii*) Despite the tolerance of the approach for generating BGBs with respect to wavelengths, the diffraction of laser beams with broad spectra (e.g., femtosecond beams/pulses) is more strongly affected by this truncation than the diffraction of relatively narrow-bandwidth picosecond beams. Our specific data show a ratio of these increments for fs mode to ps mode equal to 1.5 at the maximum beam propagation distance in this experiment (z = 4.75 m).

In Figure 4, we show the experimentally recorded energy density distributions at the largest propagation distance of 4.7 m in this experiment, just 35 cm farther from the position at which the data presented in Figures 2 and 3 are recorded. In the upper-left panel in Figure 4 marked with "G", we show the Gaussian background beam as observed with the femtosecond laser beam. Unfortunately, at the same position, the background beam from the picosecond laser only partially fitted on the CCD camera sensor. It was possible to reliably register it 1.35 m behind the focal plane of the lens only. Despite this significant difference between the sizes and divergences of the background beams, the comparison between the BGBs in the two modes (see the first column of frames in Figure 4) shows a minimal difference. In the picosecond mode, the rings around the central peak have a slightly deeper modulation than in the femtosecond mode. In both pulse regimes, at the fixed propagation length z = 4.7 m, the increased truncation of the satellite dark rings leads to an increased broadening of the central peaks. This is consistent with the data on the diffraction of equally truncated beams in both modes, summarized in Table 1. Although not large, the difference in the diffraction of identically truncated beams in the two modes is accompanied by relatively smaller deformation of the first satellite bright ring and by weaker broadening of the central peak of the beam generated in the picosecond regime. However, these observations are consistent with the conclusions formulated in points (*i*) and (*ii*) above, related to Figures 2 and 3.

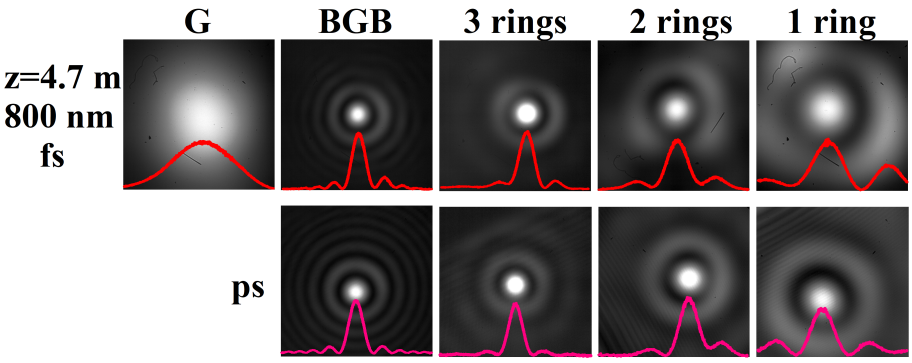

Figure 4. Energy density distributions of the unperturbed Gaussian background beam (upper-left panel marked with G), of the generated Bessel-Gaussian beams (column marked with BGB), and of the TBGBs with 3, 2, and 1 rings, when broadband sub-7-femtosecond pulses (upper row of panels) and relatively narrow-bandwidth picosecond pulses are used (lower row of frames). In both cases, the central wavelength of the spectra (800 nm) matches the design wavelength of the used VP. All data are recorded at a propagation distance of 4.7 m. Inset red curves—radial cross-sections of the energy density distributions.

The results shown in Figure 5 are obtained at a much shorter wavelength of 430 nm, which is close to the second harmonic of 800 nm. Unfortunately, for the used laser (Fianium), this wavelength was the minimum that could be reached. Due to its relatively low laser output power at 430 nm, the experimental data, especially at longer propagation distances, are noisier (see graph (c) in Figure 5). The importance of this measurement stems from the fact that, at a wavelength almost twice smaller than the design wavelength for the VP, the VP generates (fractional) OVs with a twice higher topological charge of 8 (i.e., $|TC| = 16$). As mentioned and shown in detail in [15], after double passage through this VP and subsequent focusing, high-quality BGBs are generated. In this case, due to the higher TC, the stronger repulsion between the optical vortices "opens up" a wider bright ring in the background beam (see Figure 2 in [13]). As a result, its Fourier transformation leads to a narrower central peak of the BGB (see Figures 1 and 6a in [14]). This is clearly seen by comparing the BGBs (marked with red curves and corresponding hollow circles) in graphs (a) in Figure 3 for 800 nm and in Figure 5 for 430 nm.

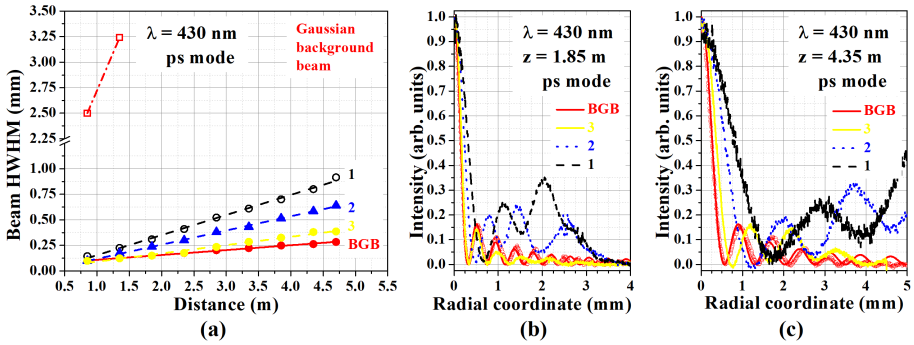

Figure 5. Results obtained with picosecond laser pulses emitted at a wavelength $\lambda = 430$ nm. The same focusing lens and the same VP are used. (**a**)—Beam divergences of the generated BGB (red solid circles) and of the TBGBs with 3 (yellow solid circles/line), 2 (blue dashed line and solid triangles), and 1 satellite ring (black dashed line and open circles). Dash-dotted line and open squares—the significantly higher divergence of the unmodulated Gaussian background beam. (**b**,**c**)—Normalized radial cross-sections of the BGB and of the TBGBs for propagation distances z = 1.85 m and z = 4.35 m behind the lens focal plane.

In this case, using a laser beam emitted at 430 nm, the aforementioned trends can be observed again: (*iii*) The decrease in the number of rings around the central peak of

the TBGB leads to an increase in its divergence (graph (a) in Figure 5), and (*iv*) with three satellite rings, the radial cross-sections of the TBGB do not differ noticeably from those of the undisturbed BGB, but their reduction to two or even to one satellite dark ring leads to a significant degradation of the transverse structure of the beam (see graphs (b) and (c) in Figure 5).

In Figure 6, we show results for λ = 1100 nm. This wavelength is at the upper limit of the spectral range within which it was possible to tune the acousto-optic filter of the used laser (Fianium). Both wavelengths 430 nm and 1100 nm differ significantly from the design wavelength of the used VP (800 nm). Therefore, the optical vortices generated using this VP have lower and fractional topological charges (i.e., their rings are non-negligibly azimuthally perturbed). The already-mentioned wavelength tolerance of the method [15] we use to generate long-range BGBs is also manifested positively here (as will be discussed in connection to Figure 7). The significant difference from the results obtained at the correct wavelength 800 nm is that the number of satellite dark rings is crucial for the evolution of the central peak. Due to the strong azimuthal modulation of the second, third, and other more distant rings, in Figure 6b,c, we show the radial cross-sections of the BGBs with all (even perturbed) rings (red hollow circles and red solid lines) and with only one first remaining ring around the central peak (black solid curves). It can be seen that when the entire rich (albeit modulated) peripheral structure is present around the central peak, the BGB has good modulation depth at the first satellite dark ring. Cutting it down to only one satellite ring significantly degrades the modulation. This leads to the conclusion that, even in the first satellite dark ring, the radial π-phase jumps are absent. As a result of the radial energy transfer, and probably intensified by the stronger diffraction of the central peak at this longer wavelength (see graph (a) in Figure 6), the intensity of the first satellite bright ring increases noticeably (graph (c) in Figure 6). The decay of the central peak also is more strongly pronounced compared with the case in which the rich (and modulated) peripheral ring structure is present. At a qualitative level, from these results we can conclude that, in BGBs formed by the decay and annihilation of OVs with fractional topological charges, the presence of a (even modulated) peripheral structure of satellite rings is essential for the low divergence and for the stable propagation of the central peak of the generated BGBs.

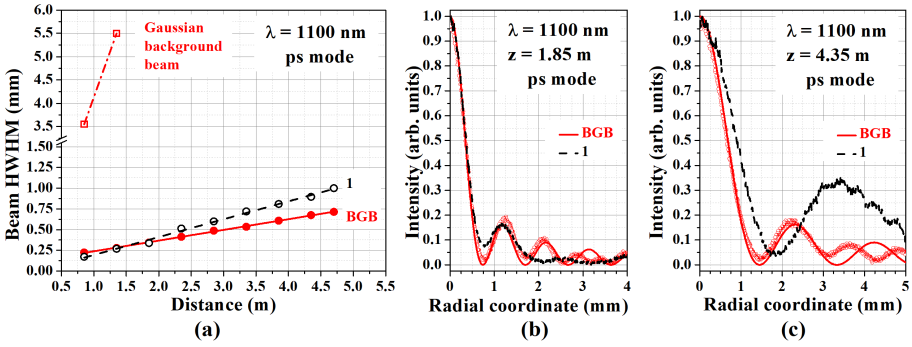

Figure 6. Results obtained with picosecond laser pulses emitted at λ = 1100 nm. (**a**)—Beam divergences of the generated BGB (red solid circles) and of the TBGB with 1 satellite ring (black dashed line and open circles). Dash-dotted line and open squares—divergence of the unmodulated Gaussian background beam. (**b**,**c**)—Normalized radial cross-sections of the BGB and the TBGB with 1 ring for distances z = 1.85 m and z = 4.35 m behind the lens focal plane.

In Figure 7, we compare the energy density distributions of BGBs and of TBGBs at three wavelengths extracted from the Fianium laser in ps mode. Comparing the data in the left column of frames, it can be seen that the decrease in wavelength leads to narrower central peaks of theBGBs and to a larger number of well-defined coaxial rings surrounding them. This is a result of the higher TCs of the initially generated and subsequently annihi-

lated OVs and the corresponding wider ring-shaped beams in the plane of the focusing lens. At λ = 1100 nm, the fractional TCs of the vortices are seen to lead to a non-negligible modulation of the second and more distant satellite rings. For this reason, energy density distributions of TBGBs with 2 and 3 rings are intentionally not presented. In the last row of Table 1, the two respective cases are marked as not available (n.a.). With the remaining 3 satellite rings, the spatial distribution of the TBGB generated at the design wavelength of the VP (800 nm) is relatively the best. Although there are significant deformations and increased divergence, this remains the case for filtered 2 and 1 dark rings.

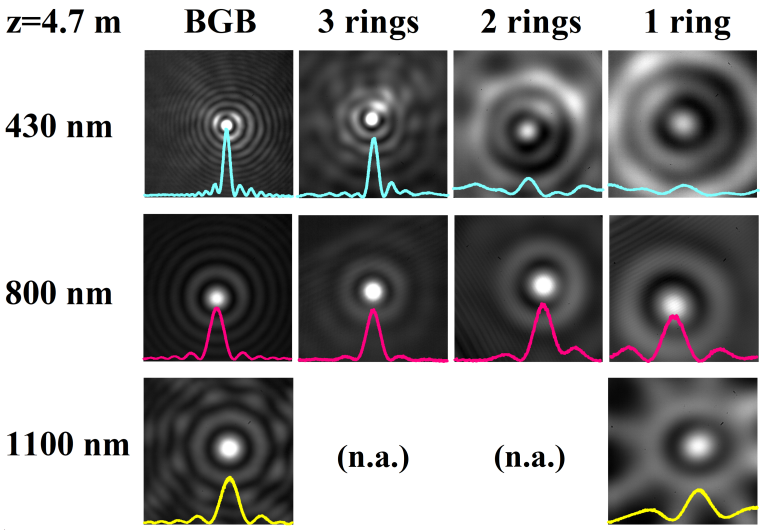

Figure 7. Energy density distributions of the analyzed BGBs (left column of frames) and of BGBs with truncated coaxial rings (see the notations above the columns of frames), generated using laser emission at 430 nm (upper row of frames), 800 nm (middle, ps pulses), and 1100 nm (lower row of frames) recorded at a propagation distance z = 4.7 m.

Due to the relatively large number of experimental results worth presenting, we have organized them into four figures and included them in the Supplementary Materials to this paper.

The data presented in Table 2 are indicative of the order of magnitude of the divergences of the central peaks of the undisturbed BGBs, for which the truncation of the satellite rings has no noticeable effect. To obtain BGBs with diffraction angles of the order of milliradians (i.e., of the order of diffraction angles of relatively high-quality unmodulated Gaussian beams), we used a lens with a shorter focal length—f = 15 cm instead of f = 50 cm, used up to now. All other experimental parameters are the same as those used to obtain the data in Table 1. Since the maximum truncation of the satellite rings is up to 1 dark/bright ring around the central peak of the BGBs, Table 2 presents data only for the divergences of the beams in this extreme case. They are compared with the propagation of the BGBs when they carry their entire rich (even modulated) structure of rings. Looking at the data for each wavelength separately shows that, within the error in calculating the diffraction angles, the data for the non-truncated BGBs are practically the same as those for the TBGBs. In the case of 7 fs pulses emitted at the "correct" wavelength of 800 nm for the used VP, the divergence angles of the BGBs and TBGBs are higher than those in Table 1. A possible explanation for this is the stronger spatial localization of the central peak of the beam with this ≈3.3 times shorter-focus lens, and hence the stronger influence of diffraction. From the data, it can be concluded that the diffraction of central peaks of the TBGBs is influenced by the degree of cutting of the satellite rings for the central peak when the diffraction angles of the central peaks of the BGBs are of the order of 100 μrad or less. This means that, keeping all other conditions unchanged, the influence of the truncation of the satellite rings will be more pronounced when using relatively longer-focus Fourier-transforming lenses, achieving

longer propagation distances at lower diffraction angles. More generally, the truncation effect is significant only when the BGB itself has a sufficiently small divergence (on the microradian scale).

Table 2. Retrieved divergences of the central peaks of the Bessel-Gaussian beams (BGBs) and the truncated BGBs (TBGBs) with one satellite ring for four different wavelengths. In contrast with the data shown in Table 1, the focal length of the used Fourier-transforming lens is shorter—f = 15 cm. All other experimental conditions are the same. The standard errors of the respective linear fits are given in brackets.

Divergence Half Angle [μrad] for f = 15 cm		
Wavelength	**BGB**	**1 Ring**
430 nm (ps)	567 (±4)	587 (±16)
800 nm (ps)	1020 (±6)	983 (±33)
800 nm (fs)	1210 (±10)	1200 (±11)
1100 nm (ps)	1150 (±7)	1090 (±15)

3. Conclusions

In this article, we presented experimental evidence that, under otherwise identical experimental conditions, the number of bright ring-shaped waves and the π-phase jumps between them have a significant influence on the divergence of the central peak of zero-order Bessel-Gaussian beams, when the undisturbed Bessel-Gaussian beam has a divergence of the order of microradians. The ability to control it is not significantly affected by how well the used wavelength matches the wavelength for which the phase plates are designed. This truncation of the coaxial rings of Bessel-Gaussian beams works for both beams/pulses with relatively narrow spectra and for broadband radiation emitted by femtosecond lasers. This method could appear useful in free space optical communications, for example, to control the security of data transfers.

Supplementary Materials: The following supporting information can be downloaded at: https://www.mdpi.com/article/10.3390/photonics13050483/s1, Figure S1: Picosecond pulses at λ = 430 nm. Energy density distributions of Bessel-Gaussian beam (BGB) and of truncated BGBs with 3, 2, and 1 rings, recorded at three propagation distances z measured from the focal plane of the focusing lens. For better visibility, each frame (1200 pix. × 1200 pix.) is adjusted in brightness; Figure S2: Femtosecond pulses at λ = 800 nm. Energy density distributions of Bessel-Gaussian beam (BGB) and of truncated BGBs with 3, 2, and 1 rings, recorded at three propagation distances z measured from the focal plane of the focusing lens. For better visibility, each frame (1200 pix. × 1200 pix.) is adjusted in brightness; Figure S3: Picosecond pulses at λ = 800 nm. Energy density distributions of Bessel-Gaussian beam (BGB) and of truncated BGBs with 3, 2, and 1 rings, recorded at three propagation distances z measured from the focal plane of the focusing lens. For better visibility, each frame (1200 pix. × 1200 pix.) is adjusted in brightness; Figure S4: Picosecond pulses at λ = 1100 nm. Energy density distributions of Bessel-Gaussian beam (BGB) and of truncated BGB with 1 ring, recorded at three propagation distances z measured from the focal plane of the focusing lens. For better visibility, each frame (1200 pix. × 1200 pix.) is adjusted in brightness; Figure S5: Energy density distributions of OV beams generated from a Gaussian beam passing ones through a vortex phase plate designed and fabricated for 800 nm with a topological charge $|TC| = 8$. The respective wavelength λ of the used picosecond beam and the retrieved ring radius-to-arc width ratio r_0/ω_0 are listed for each frame.

Author Contributions: Conceptualization, N.D. and A.D.; experimental investigation, N.D.; data curation, N.D.; writing—original draft preparation, A.D. and M.Z.; writing—review and editing, N.D., M.Z. and A.D.; supervision, A.D. All authors have read and agreed to the published version of the manuscript.

Funding: We acknowledge funding from the Bulgarian National Science Fund (project КП-06-Н78/6). N.D. and A.D. were also supported by the European Union NextGenerationEU through the "National Recovery and Resilience Plan of the Republic of Bulgaria, project BG-RRP-2.004-0008-C01". We acknowledge support from the Science Fund of Sofia University (grant 80-10-49/06.04.2026). This work was also supported by the Bulgarian Ministry of Education and Science as part of the National Roadmap for Research Infrastructure, project DO1-102/26.06.2025 (ELI ERIC BG) and by the European Regional Development Fund under the "Research Innovation and Digitization for Smart Transformation" program 2021–2027 under project BG16RFPR002-1.014-0006, "National Centre of Excellence Mechatronics and Clean Technologies".

Data Availability Statement: The datasets generated and analyzed during the current study are available from the corresponding author upon reasonable request.

Conflicts of Interest: The authors declare no conflicts of interest.

References

1. Durnin, J. Exact solutions for nondiffracting beams. I. The scalar theory. *J. Opt. Soc. Am. A* **1987**, *4*, 651–654. [CrossRef]
2. Khonina, S.N.; Ustinov, A.V.; Chávez-Cerda, S. Generalized parabolic nondiffracting beams of two orders. *J. Opt. Soc. Am. A* **2018**, *35*, 1511–1517. [CrossRef]
3. Stoyanov, L.; Topuzoski, S.; Paulus, G.G.; Dreischuh, A. Optical vortices in brief: Introduction for experimentalists. *Eur. Phys. J. Plus* **2023**, *138*, 702. [CrossRef]
4. Vetter, C.; Steinkopf, R.; Bergner, K.; Ornigotti, M.; Nolte, S.; Gross, H.; Szameit, A. Realization of Free-Space Long-Distance Self-Healing Bessel Beams. *Laser Photonics Rev.* **2019**, *13*, 1900103. [CrossRef]
5. Stoyanov, L.; Zhang, Y.; Dreischuh, A.; Paulus, G.G. Long-range quasi-non-diffracting Gauss-Bessel beams in a few-cycle laser field. *Opt. Express* **2021**, *29*, 10997–11008. [CrossRef]
6. Durnin, J.; Miceli, J.J.; Eberly, J.H. Diffraction-free beams. *Phys. Rev. Lett.* **1987**, *58*, 1499–1501. [CrossRef] [PubMed]
7. Duocastella, M.; Arnold, C. Bessel and annular beams for materials processing. *Laser Photonics Rev.* **2012**, *6*, 607–621. [CrossRef]
8. Mahmoud, M.A.; Shalaby, M.Y.; Khalil, D. Propagation of Bessel beams generated using finite-width Durnin ring. *Appl. Opt.* **2013**, *52*, 256–263. [CrossRef]
9. Indebetouw, G. Nondiffracting optical fields: Some remarks on their analysis and synthesis. *J. Opt. Soc. Am. A* **1989**, *6*, 150–152. [CrossRef]
10. McGloin, D.; Dholakia, K. Bessel beams: Diffraction in a new light. *Contemp. Phys.* **2005**, *46*, 15–28. [CrossRef]
11. Shen, T.; Lang, T.; Wu, M.; Han, Z. Bessel-like beam generated by an axicon based on parallel-plate waveguides. *Appl. Opt.* **2018**, *57*, 6174–6180. [CrossRef]
12. Yu, X.; Todi, A.; Tang, H. Bessel beam generation using a segmented deformable mirror. *Appl. Opt.* **2018**, *57*, 4677–4682. [CrossRef] [PubMed]
13. Stoyanov, L.; Zhekova, M.; Stefanov, A.; Stefanov, I.; Paulus, G.G.; Dreischuh, A. Zeroth- and first-order long range non-diffracting Gauss–Bessel beams generated by annihilating multiple-charged optical vortices. *Sci. Rep.* **2020**, *10*, 21981. [CrossRef]
14. Stoyanov, L.; Zhekova, M.; Stefanov, A.; Ivanov, B.; Stefanov, I.; Paulus, G.G.; Dreischuh, A. Generation of long range low-divergent Gauss–Bessel beams by annihilating optical vortices. *Opt. Commun.* **2021**, *480*, 126510. [CrossRef]
15. Stoyanov, L.; Dimitrov, N.; Wiesner, F.; Fedoruk, M.; Paulus, G.G.; Dreischuh, A. Wavelength-tolerant generation of Bessel-Gaussian beams using vortex phase plates. *Appl. Opt.* **2024**, *63*, 5699–5705. [CrossRef]
16. Zhang, N.; Ye, J.S.; Feng, S.F.; Wang, X.K.; Han, P.; Sun, W.F.; Zhang, Y.; Zhang, X.C. Generation of long-distance stably propagating Bessel beams. *OSA Contin.* **2021**, *4*, 1223–1233. [CrossRef]
17. Gao, L.; Shao, L.; Chen, B.C.; Betzig, E. 3D live fluorescence imaging of cellular dynamics using Bessel beam plane illumination microscopy. *Nat. Protoc.* **2014**, *9*, 1083–1101. [CrossRef]
18. Garcés-Chávez, V.; McGloin, D.; Melville, H.; Sibbett, W.; Dholakia, K. Simultaneous micromanipulation in multiple planes using a self-reconstructing light beam. *Nature* **2002**, *419*, 145–147. [CrossRef]
19. McKell, C.; Bonin, K.D. Optical corral using a standing-wave Bessel beam. *J. Opt. Soc. Am. B* **2018**, *35*, 1910–1920. [CrossRef]
20. Oosterbeek, R.N.; Ashforth, S.; Bodley, O.; Simpson, M.C. Measuring the ablation threshold fluence in femtosecond laser micromachining with vortex and Bessel pulses. *Opt. Express* **2018**, *26*, 34558–34568. [CrossRef]
21. Gailevičius, D.; Purlys, V.; Staliunas, K. Photonic crystal spatial filters fabricated by femtosecond pulsed Bessel beam. *Opt. Lett.* **2019**, *44*, 4969–4972. [CrossRef] [PubMed]
22. Kumar, S.; Eaton, S.M.; Bollani, M.; Sotillo, B.; Chiappini, A.; Ferrari, M.; Ramponi, R.; Di Trapani, P.; Jedrkiewicz, O. Laser surface structuring of diamond with ultrashort Bessel beams. *Sci. Rep.* **2018**, *8*, 14021. [CrossRef]

23. Meyer, R.; Jacquot, M.; Giust, R.; Safioui, J.; Rapp, L.; Furfaro, L.; Lacourt, P.A.; Dudley, J.M.; Courvoisier, F. Single-shot ultrafast laser processing of high-aspect-ratio nanochannels using elliptical Bessel beams. *Opt. Lett.* **2017**, *42*, 4307–4310. [CrossRef]
24. Bhuyan, M.K.; Courvoisier, F.; Lacourt, P.A.; Jacquot, M.; Salut, R.; Furfaro, L.; Dudley, J.M. High aspect ratio nanochannel machining using single shot femtosecond Bessel beams. *Appl. Phys. Lett.* **2010**, *97*, 081102. [CrossRef]
25. Bhuyan, M.K.; Courvoisier, F.; Phing, H.S.; Jedrkiewicz, O.; Recchia, S.; Di Trapani, P.; Dudley, J.M. Laser micro- and nanostructuring using femtosecond Bessel beams. *Eur. Phys. J. Spec. Top.* **2011**, *199*, 101–110. [CrossRef]
26. Li, M.; Tang, X.; Wang, H.; Li, J.; Wang, W.; Cai, J.; Zhang, J.; San, X.; Zhao, X.; Ma, P.; et al. Efficient generation of Bessel-Gauss attosecond pulse trains via nonadiabatic phase-matched high-order harmonics. *Light. Sci. Appl.* **2025**, *14*, 181. [CrossRef]
27. Mphuthi, N.; Gailele, L.; Litvin, I.; Dudley, A.; Botha, R.; Forbes, A. Free-space optical communication link with shape-invariant orbital angular momentum Bessel beams. *Appl. Opt.* **2019**, *58*, 4258–4264. [CrossRef] [PubMed]
28. Li, S.; Wang, J. Adaptive free-space optical communications through turbulence using self-healing Bessel beams. *Sci. Rep.* **2017**, *7*, 43233. [CrossRef] [PubMed]
29. Grunwald, R.; Bock, M. Needle beams: A review. *Adv. Phys.* **2020**, *5*, 1736950. [CrossRef]
30. Yan, Q.; Zhao, S.; Guo, X.; Chen, T.; Ming, M. Design of diffractive optical elements to suppress the Bessel-Gauss beam generated by reflective off-axis axicon. *Res. Phys.* **2026**, *80*, 108550. [CrossRef]